# OPD measurement and dispersion reduction in a monolithic interferometer

**Brian Hicks,**[1,*] **Timothy Cook,**[1] **Benjamin Lane**[2] **and Supriya Chakrabarti**[1]

[1]*Center for Space Physics, Boston University, 725 Commonwealth Avenue, Boston, MA 02215, USA*

[2]*Draper Laboratory, 555 Technology Square, Cambridge, MA 02139, USA*

*bahicks@bu.edu

**Abstract:** We describe a white light fringe scanning and pupil bisecting method of measuring the optical path difference (OPD) between arms of a monolithic nulling interferometer that is designed to enable direct imaging of planetary companions and the environments around nearby stars. This measurement is used to determine the differential thicknesses of optically contacted compensator plates used to reduce OPD, which can drastically impair the optic's performance in broadband light. By making this correction, we were able to reduce the initial OPD from $949 \pm 44$ nm to $63 \pm 10$ nm. In the absence of any other asymmetries that can compromise the null, such a correction corresponds to an increase in an R-band ($\lambda_c = 648$nm) nulling bandpass from monochromatic to 25%.



**OCIS codes:** (120.3180) Interferometry; (120.2650) Fringe analysis; (220.4610) Optical fabrication; (260.3160) Interference; (260.2030) Dispersion; (350.1260) Astronomical optics.

## References and links

1. G. G. Shepherd, G. Thuillier, W. A. Gault, B. H. Solheim, C. Hersom, J. M. Alunni, J. Brun, S. Brune, P. Charlot, and L. L. Cogger, "WINDII, the wind imaging interferometer on the Upper Atmosphere Research Satellite," J. Geophys. Res. **98**, 10725–10750 (1993).
2. J. Harlander, F. Roesler, C. Englert, J. Cardon, R. Conway, C. Brown, and J. Wimperis, "Robust monolithic ultraviolet interferometer for the SHIMMER instrument on STPSat-1," Appl. Opt. **42**, 2829–2834 (2003).
3. R. N. Bracewell, "Detecting nonsolar planets by spinning infrared interferometer," Nature (London) **274**, 780–781 (1978).
4. Guyon, O., Pluzhnik, E. A., Kuchner, M. J., Collins, B., & Ridgway, S. T., "Theoretical Limits on Extrasolar Terrestrial Planet Detection with Coronagraphs," Astrophys. J. Suppl. Ser. **167**, 81–99 (2006).
5. R. Samuele, J. Wallace, E. Schmidtlin, M. Shao, B. Levine, and S. Fregoso, "Experimental progress and results of a visible nulling coronagraph," in "Aerospace Conference, 2007 IEEE," (2007), pp. 1–7.
6. R. O. Gappinger, R. T. Diaz, A. Ksendzov, P. R. Lawson, O. P. Lay, K. M. Liewer, F. M. Loya, S. R. Martin, E. Serabyn, and J. K. Wallace, "Experimental evaluation of achromatic phase shifters for mid-infrared starlight suppression," Appl. Opt. **48**, 868–880 (2009).
7. B. Hicks, T. Cook, B. Lane, and S. Chakrabarti, "Monolithic achromatic nulling interference coronagraph: design and performance," Appl. Opt. **48**, 4963–4977 (2009).
8. B. A. Hicks, T. A. Cook, B. F. Lane, C. B. Mendillo, P. Jung, and S. Chakrabarti, "The Monolithic Achromatic Nulling Interference Coronagraph (MANIC) testbed," Proc. SPIE **7440** (2009).
9. D. Ren and E. Serabyn, "Symmetric nulling coronagraph based on a rotational shearing interferometer," Appl. Opt. **44**, 7070–7073 (2005).
10. E. Serabyn, "Nulling interferometry: symmetry requirements and experimental results," Proc. SPIE **4006**, 328–339 (2000).
11. Heraeus Quartz America, L.L.C, "Quartz Glass for Optics Data and Properties," http://www.wilmad-labglass.com/pdf/Heraeus_Quartz_Properties.pdf (accessed 2010).
12. E. Friedman and J. L. Miller, *Photonics Rules of Thumb* (McGraw-Hill, 2003).

#130149 - $15.00 USD Received 14 Jun 2010; revised 27 Jul 2010; accepted 28 Jul 2010; published 30 Jul 2010

## 1. Introduction

Monolithic optical systems [1, 2] have a few distinct advantages over systems assembled from discrete elements. The greatest advantages to monolithic optics are mechanical stability and reduced sensitivity to turbulence, both of which are critical for precision fringe measurement in interferometers. In high-contrast broadband nulling interferometers (nullers) conceived for exoplanet detection [3], absolute control over OPD is paramount.

Nuller development has progressed significantly in the past decade, particularly for the single aperture variety, whereby the interferometer internally makes two copies of a single input wavefront and then nulls on-axis sources by destructively interfering them while transmitting the light from off-axis sources. The various methods by which a $\pi$-phase delay is introduced for destructive interference are discussed in [4]. Contrast suppresion (nulls) have been demonstrated in the visible using shearing at the $10^7$ and $10^6$ levels for monochromatic and 15% bandpass light, respectively [5]. A mid-infrared null centered on 9.5 μm exceeding $10^4$ with a 25% bandpass is reported using field-flipping in [6].

The monolithic achromatic nulling interference coronagraph (MANIC) is an optic designed to achieve broadband $10^6$ nulls of stars in order to image objects in their immediate environment [7, 8]. MANIC nulls by means of geometric field flips about orthogonal axes, and is based on a fully symmetric rotational shearing interferometer (RSI) layout [9]. A throrough review of MANIC's heritage and an in-depth description of its operational principles are presented in [7]. In brief, MANIC consists of pairs of fused silica rhomboid, Porro, and rectangular prisms, and a cubic beamsplitter that are optically contacted to form a single element nuller (see Fig. 1). The Porro prisms produce the orthogonal electric field inversions, the rhomboid prisms balance s- and p-plane reflections between arms, and the rectangular prisms eliminate air/glass interfaces. Monolithic stability and achromatic performance, MANIC's key features, are both highly desirable qualities for a nulling interferometer. Achromatic performance for a (geometric) nulling RSI, however, assumes that the interferometer is operating at zero OPD, which is a formidable challenge to meet in fabrication of the monolith.

This work describes a method for reducing OPD initially built into the monolith in order to limit this null leakage source to a tolerable level. While there are a number of other leakage sources that must be dealt with in the design of a nuller (see e.g. [10]), they are small compared to the built-in OPD. To measure the OPD internal to MANIC, we adopt a strategy of injecting it with a bisected, fixed intensity beam and controlling the phase between the two bisected beam halves by means of a delay line. The intensity in the two halves of MANIC's output will modulate in phase if the internal path difference between its arms is zero, and out of phase proportional to the extent to which it is not.

## 2. Theory

In any nuller, static aberrations and low frequency path instabilties must be reduced to a tolerable fraction of the operating wavelength, $\lambda$, typically to a length on the order of

$$\sigma_d \approx A\lambda\sqrt{L_d}/(2\pi), \tag{1}$$

where $A$ is a dimensionless geometric factor (of order 1) that depends on the nuller design and $L_d$ is null leakage (i.e. the amount of light from the star transmitted into the detector field of view, which must be less than or comparable to planet/star contrast) attributed to OPD [10]. This can be done using active or adaptive optics (AO), commonly in the form of one or more tip/tilt/piston mirrors or deformable mirrors (DMs) paired with a wavefront sensor. For a discrete-element interferometer this can be built into one arm of the interferometer to provide piston control. For a monolithic nuller such as MANIC, wavefront correction must be

#130149 - $15.00 USD Received 14 Jun 2010; revised 27 Jul 2010; accepted 28 Jul 2010; published 30 Jul 2010

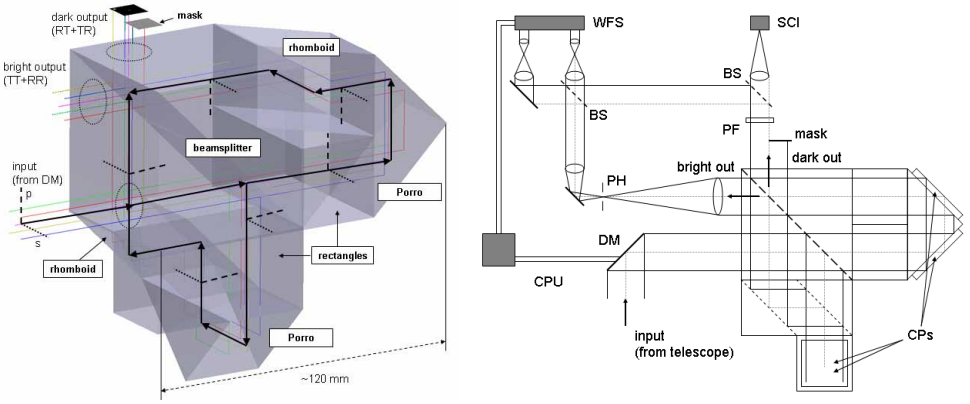


Fig. 1. MANIC (*left*) and a schematic of an AO-enabled nulling configuration (*right*) showing CPs optically contacted to the Porro prisms. The details of the AO scheme and half-pupil mask shown here are beyond the scope of this work (see [7] for details).

performed at the input (see Fig. 1). We note that in order to correct in front of a monolithic interferometer, pupil locations must be remapped, e.g. by lateral or rotational shearing in the inteferometer. If the beam pupil locations do not change, as in the case of the simple Michelson interferometer, then an equal amount of phase delay at the input would be imparted to both arms at the same recombination location having no effect.

The primary issue with correction of internal OPD at the input is refractive index mismatch. This is because the path difference to be corrected is in the nuller material (Homosil) and the correction is in air. An expression for the total chromatic leakage due to residual path error in the monolith, $l_g$ over a given bandpass, $B$, may be adapted from work presented in [7]:

$$L_{OPD} = \int_B 1 - \cos\left[\frac{2\pi l_g}{\lambda}\left(n_g(\lambda) - n_a(\lambda)\frac{n_g(\lambda_c)}{n_a(\lambda_c)}\right)\right] d\lambda, \tag{2}$$

where $n_g(\lambda)$ and $n_a(\lambda)$ are the dispersion formulae of the glass and air, respectively, and $\lambda_c$ is the central wavelength at which the OPD is actively corrected. The greater the built-in path difference, the more the dispersion imbalance between propagation media will limit the deep null bandpass. For this reason MANIC is designed to operate at zero path difference. To some extent, built-in path error can be minimized in the initial fabrication by polishing the prism pairs as single prisms, cleaving them, and then assembling them as symmetric pairs. Residual OPD can then be measured and then further reduced by optically contacting to each arm compensator plates (CPs), which are essentially differential thickness etalons made from the same material as the prisms to match dispersion. Ultimately, given the dispersion of Homosil [11], the residual path error post-CP correction must be less than 100 nm in order to be capable of producing a competitive $10^6$ null (all leakage terms included) over the entire R band ($\sim$ 25% bandpass).

## 3. Pre- and post-path correction measurement and results

The layout used to measure the OPD between the two arms of the monolith is depicted schematically in Fig. 2. We designate the initially transmitted and reflected arms as T and R, respectively. A somewhat unconventional delay line scheme is used to exploit the 180° relative pupil rotation between MANIC's output beams. The delay line was formed using an alignment cube (AC) to bisect a collimated, aperture-stopped input beam into two semicircular pupils. One is sent to a static rooftop mirror assembly (SMA), the other is sent to a delay rooftop mirror assembly (DLA). Coarse delay was achieved using a combination of manual and stepper motor

#130149 - $15.00 USD Received 14 Jun 2010; revised 27 Jul 2010; accepted 28 Jul 2010; published 30 Jul 2010

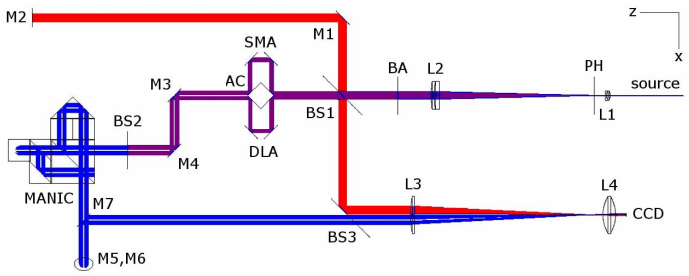


Fig. 2. Experimental setup schematic (roughly to scale) for measuring OPD internal to the monolith. The axes denote the global coordinate system. Out of plane geometry is not shown. The source is alternately a red HeNe laser used for alignment and calibrating fringe spacing, and a halogen lamp for the OPD measurement. Lens L1 focuses the source on the pinhole (PH) spatial filter. L2 collimates light from the PH. The bounding aperture (BA) sets the beam diameter. The alignment cube (AC) bisects the pupil and redirects the beam halves along static mirror assembly (SMA) and delay mirror assembly (DLA) paths. An auxiliary interferometer formed by elements BS1, BS2, and M2 is used to align the SMA and DLA in angle and path difference. Mirrors M1 and M3 through M7 are for steering.

controlled translation stages. Fine phase delay was driven by a piezoelectric transducer (PZT) translation stage. The rooftop assemblies redirected the static and delay beams (hereafter referred to and subscripted as the s and d beams) back to the alignment cube, which then directed the beams along parallel paths into the monolith.

Noting again that the geometric field inversion at the nuller output is accomplished by orthogonal field flips, the s and d beams each produce two nuller output beams: one a copy of itself flipped horizontally, the other flipped vertically (about the y- and x-axis, respectively, as denoted in Fig. 2). The mapping of these beams may be represented as:

$$\left.\begin{array}{c}\text{input}\\ (x,y)_s\\ (-x,y)_d\end{array}\right\} \Rightarrow \left\{\begin{array}{ccccc}\text{R (x-flip)} & & \text{T (y-flip)} & & \\ (-x,y)_s & + & (-x,-y)_d & \Rightarrow & \text{left null}\\ (x,y)_d & + & (-x,y)_s & \Rightarrow & \text{right null,}\end{array}\right. \tag{3}$$

where left and right null refer to the relative positions of the nuller output pupils observed on the monitor. It should be noted that the a change of sign from the left to right side of the above map indicates a reversal of pupil location at the output relative to the input for a given beam.

An auxilliary alignment and phasing interferometer (shown in red and purple in Fig. 2) was included in the optical layout to ensure that the phase delayed beams were parallel when injected into the monolith. The zero OPD search space was increased by tilting M2 to produce a high fringe count across the auxilliary interferometer pupil. After completing these steps, the laser was replaced with a halogen source. The SMA and DLA were then successively positioned at zero OPD relative to M2 in order to make white light fringes observable in either half of the auxilliary interferometer pupil (see Fig. 3). Once the beams were aligned and coarsely phased, the DLA was scanned with a long period triangle wave signal. Images of the time varying intensities were taken over many scan periods to mitigate environmental effects.

To determine the white light fringe spacing in physical units, a small amount of tilt was added to the input beams such that the fringe pattern observed in the nuller output resembled those observed in the auxiliary interferometer shown in Fig. 3. Images of the fringes produced by the halogen source, and then the red HeNe were recorded. The pixel intensities were summed in each row in one nuller output pupil half for both light sources in order to generate a 1D intensity signal versus row number. Peaks were then located in the Fourier transforms of these signals to calculate per pixel fringe spacings, $\zeta_{\text{halogen}}$ and $\zeta_{632.8}$, the ratio of which is used to recover the white light central wavelength,

#130149 - $15.00 USD Received 14 Jun 2010; revised 27 Jul 2010; accepted 28 Jul 2010; published 30 Jul 2010

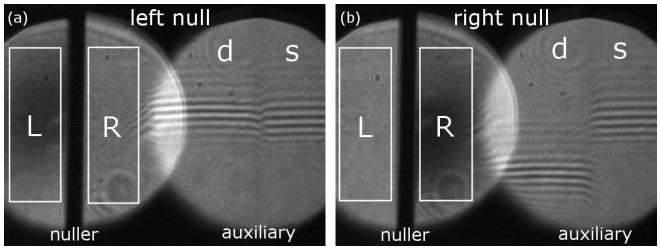


Fig. 3. Each detector image shows the nuller (low frequency fringes) and the auxiliary interferometer (high frequency fringes) output. In image (a) the left side of the nuller output (bounding box labled L) is nulled, the right side of the nuller output (bounding box labeled R) is near the midfringe intensity, and the fringe patterns in the auxiliary interferometer (labeled d and s for delay and static, respectively) appear to be nearly aligned. Note that only partial fringes are sampled inside the bounding boxes. In image (b) the delay line is positioned to null the right half of the nuller output, whereas the left null bounding box intensity is near midfringe. The shift in the delay line is evidenced by the downward shift of its fringes from image (a) to (b).

$$\lambda_{o,c} \approx \lambda_{HeNe}\zeta_{\text{halogen}}/\zeta_{632.8}, \tag{4}$$

Here we note that the ratio of the refractive index of Homosil over the spectral range of the source varies on the order of 0.4% with respect to its index at 632.8 nm [11]. This variation is comparable to the room temperature relative temperature coefficient of air, which is on the order of $10^{-3}$ K$^{-1}$ [12], but significantly exceeds Homosil's quoted room temperature relative temperature coefficient of $1.5\times10^{-5}$ K$^{-1}$ [11]. The above assumption yields an uncertainty in the measured OPD that scales with the actual remaining OPD.

To determine the OPD the intensity within a bounding box in each nuller output pupil half was measured for each frame as the delay line was scanned. Intensity functions from two measurements are plotted in Fig. 4. One is a measurement of the OPD to be corrected by the CPs, the other is the residual OPD following correction. The effect of having added the CPs on the fringe packet offset between the two measurements is clear. In the measurement taken before correcting the OPD, the packets are offset by multiple fringes. After correction, the fringe packets are almost in direct overlap.

The overall relative phase differences, $\Delta_{\text{left}}$ and $\Delta_{\text{right}}$, between interfering beams observed in the nuller outputs depend on the differing paths traversed prior to injection, $l_s$ and $l_d$, and internal to the monolith, $l_R$ and $l_T$, all of which follow the same subscript designation described in the text around Eq. (3), and are related by:

$$\Delta_{\text{left}} = (\phi_d+\phi_R)-(\phi_s+\phi_T) = 2\pi[(l_d-l_s)+n_{g,\lambda_{o,c}}(l_R-l_T)]/\lambda_{o,c} \tag{5a}$$

$$\Delta_{\text{right}} = (\phi_d+\phi_T)-(\phi_s+\phi_R) = 2\pi[(l_d-l_s)+n_{g,\lambda_{o,c}}(l_T-l_R)]/\lambda_{o,c} \tag{5b}$$

where subscripted $\phi$ corresponds to the phase contribution from the delay lines and monolith arms and $n_{g,\lambda_{o,c}}$ is glass' index at the wavelength that corresponds to the fringe spacing, $\lambda_{o,c}$.

As a nuller, the central fringe minima in the nuller output pupil halves occur at accumulated phase delays of $\Delta_{\text{left}}=0$ and $\Delta_{\text{right}}=0$, which occurs when the only free parameter in Eq. (5), the delay path length $l_d$ equals $l_{\text{left}}$ and $l_{\text{right}}$, respectively. In this case, we may write

$$n_{g,\lambda_{o,c}}(l_R-l_T) = (l_{\text{left}}-l_s) \tag{6a}$$

$$n_{g,\lambda_{o,c}}(l_T-l_R) = (l_{\text{right}}-l_s). \tag{6b}$$

which when subtracted yield the result

$$n_{g,\lambda_{o,c}}(l_R-l_T) = (l_{\text{left}}-l_{\text{right}})/2. \tag{7}$$

#130149 - $15.00 USD Received 14 Jun 2010; revised 27 Jul 2010; accepted 28 Jul 2010; published 30 Jul 2010

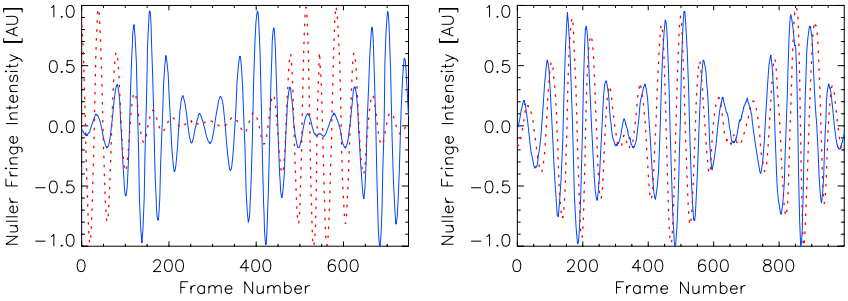


Fig. 4. Two nuller output intensity functions (solid and dotted curves) are generated from a series of detector images (e.g. those shown in fig. (3)), each corresponding to a different location in a slow sawtooth scan of the DLA performed before (*left*) and after (*right*) attaching CPs. The two plots above show three sets of traces through the white light fringes observed in each half of the nuller output. The number of frames between the fringe packet minima for each set (approximately 120 and 10 frames for each set in the left and right plots, respectively) are used with the fringe frequency and central wavelength to recover the residual OPD in the optic, pre- and post-correction as described in Eq. (8).

Since, however, we are not directly measuring physical paths, rather fringe offsets and frequencies, we rewrite Eq. (7) as

$$n_{g,\lambda_{o,c}}(l_R - l_T) = \lambda_{o,c}\Lambda(\mathscr{L} - \mathscr{R})/2. \tag{8}$$

where $\mathscr{L}$ and $\mathscr{R}$ are the frame numbers at which the central fringe minima are observed in the left and right nuller outputs, respectively, and $\Lambda$ is the measured fringe frequency per frame.

Following multiple measurements using the analysis described above, the OPD built into the monolith was found to be $949 \pm 44$ nm. The $\sim 1$ mm thick differential thickness CPs were polished flat to $\lambda/20$ surfaces. The CPs were also fabricated from the same ingot used for the prisms in order to match material properties. After optically contacting the CPs and repeating the same measurement, the remaining OPD was measured to be $63 \pm 10$ nm. Such a post-correction residual path difference is consistent with the pre-correction measured error, a product of refractive index uncertainty, and the effects of contacting $\sim \lambda/20 \approx 30$ nm surfaces.

## 4. Conclusion

We have demonstrated a method for measuring and correcting OPD in monolithic nulling interferometers that would otherwise drastically impair broadband performance. Without such a technique, the attractive concept of a monolithic nuller, with its most desirable quality of monolithic stability, would not move forward. After the initial assembly, the OPD built into MANIC was remarkably small considering the 210 mm of non-common path traversed in the two halves of the optic. If this OPD were to be left uncorrected, however, dispersion imbalance would limit the $10^6$ null to a maximum 5% red light (R band) bandpass, whereas a $10^7$ null would effectively only be possible in monochromatic light. After attaching the CPs the OPD was reduced to a level such that, assuming no other sources of null leakage, MANIC is theoretically capable of $10^6$ and $10^7$ nulls over 50% and 25% bandpasses, respectively.


## Acknowledgements

The authors of this paper would like to acknowledge Ian Miller and Jeff Wimperis (Light-Machinery, Inc.) for many useful suggestions. MANIC is funded under NASA grants NNX07AH89G and NNG05WC17G, and Boston University Photonics Center and Massachusetts Space Grant Consortium fellowships.


#130149 - $15.00 USD Received 14 Jun 2010; revised 27 Jul 2010; accepted 28 Jul 2010; published 30 Jul 2010